

Resurrection of a superhydrophobic cylinder impacting onto liquid bath

Wanqiu Zhang¹, Yaochen Mei¹, Chenyu Fu¹ and Xinping Zhou^{1,2,†}

¹School of Mechanical Science and Engineering, Huazhong University of Science and Technology, Wuhan 430074, PR China

²State Key Laboratory of Intelligent Manufacturing Equipment and Technology, Huazhong University of Science and Technology, Wuhan 430074, PR China

(Received 25 November 2023; revised 12 June 2024; accepted 13 June 2024)

An interesting resurrection phenomenon (including the initial complete submersion, subsequent resurfacing and final rebounding) of a superhydrophobic sphere impacting onto a liquid bath was observed in experiments and direct numerical simulations by Galeano-Rios *et al.* (*J. Fluid Mech.*, vol. 912, 2021, A17). We investigate the mechanisms of the liquid entry for a superhydrophobic cylinder in this paper. The superhydrophobic cylinder, commonly employed as supporting legs for insects and robots at the liquid surface, can exhibit liquid-entry mechanisms different from those observed with the sphere. The direct numerical simulation method is applied to the impact of a two-dimensional (2-D) superhydrophobic cylinder (modelled as a pseudo-solid) onto a liquid bath. We find that for the impacting cylinder the resurrection phenomenon can also exist, and the cylinder can either rebound (get detached from the liquid surface) or stay afloat after resurfacing. The cylinder impact behaviour is classified into four regimes, i.e. floating, bouncing, resurrecting (resurrecting-floating and resurrecting-bouncing) and sinking, dependent on the Weber number and the density ratio of the cylinder to the liquid. For the regimes of floating and bouncing, the force analysis indicates that the form drag dominates the motion of the cylinder in the very beginning of the impact, while subsequently the surface tension force also plays a role with the contact line pinning on the horizontal midline of the cylinder. For the critical states of the highlighted resurrecting regime, our numerical results show that the rising height for the completely submerged cylinder of different density ratios remains nearly unchanged. Accordingly, a relation between the maximum ascending velocity and the density ratio is derived to predict whether the completely submerged cylinder can resurface.

Key words: capillary flows

† Email address for correspondence: xpzhou08@hust.edu.cn

1. Introduction

It is important to understand the statics and dynamics of bodies under the effect of gas–liquid interface in nature, ranging from standing and locomotion of insects on water (Bush & Hu 2006) through water entry of bodies (Truscott, Epps & Belden 2014) to mineral flotation (Ueda *et al.* 2010). The design of micromachines or microrobots on the gas–liquid interface is becoming increasingly popular in research, for example, processing platforms floating on a liquid surface (Bowden *et al.* 1997; Barbot *et al.* 2019; Basualdo *et al.* 2021; Jung *et al.* 2021), water walking microrobots (Hu, Chan & Bush 2003; Hu *et al.* 2018) and strider-like water jumping microrobots (Koh *et al.* 2015).

Floating and sinking are the two main states of a small object on the liquid surface in the absence of an initial velocity of the body, considering the effect of surface tension and gravity. Vella (2015) presented a review of research on floating and sinking states of a small object. A small object with larger density than water can float at the water surface under the effect of surface tension or sink in the water. Whether the state is floating or sinking is determined by some parameters, e.g. the density, size, shape and surface properties of the object, and the distance away from nearby other objects. Pierson & Magnaudet (2018) conducted experimental research on the inertial settling of a sphere through an interface between two immiscible liquids with moderate density difference, and investigated the floating and sinking regimes. In addition to different sinking modes, due to the absence of initial sphere velocity, only the static state of flotation of sphere was illuminated but the transient state of initially sinking and then floating has not been mentioned.

The impact of bodies onto liquid can lead to rich physical phenomena, which involve the inertial force, the surface tension force, the hydrodynamic force and the gravitational force. Research on this topic focuses on the impact of spherical particles onto liquid. For a relatively low impact speed, the particle may either sink into the liquid with the pulled cavity pinching off or rebound with the pulled cavity not pinching off (Chen *et al.* 2018), depending on the properties of the particle and the liquid. For a high impact speed, a region of high pressure in liquid can appear and form a splash in the early stage of the impact (Thoroddsen *et al.* 2004; Marston, Li & Thoroddsen 2012). Wagner's theory (Wagner 1932) describes this important early stage, and is often applied in many studies concerning the high-speed impact between two phases (solid–liquid or liquid–liquid), e.g. Coite & Armand (1987), Howison, Ockendon & Wilson (1991) and Cimpeanu & Moore (2018).

Recently, Galeano-Rios *et al.*'s (2021) experiments on impact of a superhydrophobic sphere onto water for three densities of particle (1.2, 2.2 and 3.2 g cm⁻³), three radii of particle (0.83, 1.24 and 1.64 mm) and different impact velocities (30–110 cm s⁻¹) found a new dynamical phenomenon that the pulled cavity pinches off and eventually the particle rebounds. This phenomenon was called resurrection, which occurs in a narrow range of impact velocities and for a sufficiently small density difference between the particle and the water. The observed resurrection was reproduced by direct numerical simulations (DNS) conducted for the particle density of 1.2 g cm⁻³. The observation of the interesting resurrection phenomenon may be crucial to the design of strider-like water jumping microrobots (Koh *et al.* 2015). Up to date, the ranges of values in main parameters for the occurrence of resurrection have not been determined due to the limited cases of experiments and more limited cases of DNS.

A strider has long cylinder-like legs, and the cylinder-like shape can increase the surface tension force in order to bear the weight of the strider and the impact especially as the strider jumps. Vella, Lee & Kim (2006) performed an experiment to investigate the descending process of a horizontal cylinder on the air–water interface, and developed a simple hydrodynamic model based on the experimental data. Using the developed

model, they predicted that the sinking time taken for the cylinder to reach the fully immersed state due to gravity is directly proportional to $\sqrt{l_{ca}/g}$ where l_{ca} is the capillary length and g is gravitational acceleration. Vella & Metcalfe (2007) developed a nonlinear two-dimensional (2-D) mathematical model of equilibrium of a floating infinite cylinder and studied the criterion for the cylinder sinking. According to Bhatnagar & Finn (2006) and Chen & Siegel (2018), a floating cylinder under the surface tension effect may reach equilibrium states, but some of these states are unstable. Janssens, Chaurasia & Fried (2017) studied a partly submerged cylinder under the effect of the surface tension imbalance and discussed the Marangoni propulsion for the floating cylinder, which possibly inspires a new way to manipulate long cylinders at the liquid–gas interface. By comparing the stabilities of confined and unconfined floating cylinders, Zhang & Zhou (2023) found the confinement by two hydrophobic plates with a small spacing can assist with the interfacial floatation of a cylinder with a larger weight.

Different from the floatation behaviour of a 2-D body, the impacting dynamical behaviour of a 2-D body or a long cylinder onto a liquid bath is much richer, dependent on the impacting velocity and the particle-to-liquid density ratio. Some experimental research about a long horizontal cylinder falling or impacting onto water was conducted. Greenhow & Lin (1983) and Greenhow (1988) experimentally observed the evolution of air–water interface as a horizontal long circular cylinder descends through the interface. Colicchio *et al.* (2009) conducted experimental and numerical investigations of the water-entry and water-exit of a light (lighter than water) circular cylinder either freely falling at a height above the interface or exiting the water at a depth below the interface. Goharzadeh & Molki (2012) designed a release unit of horizontally releasing a horizontal cylinder to make the horizontal cylinder vertically descend through the interface and experimentally observed the impact dynamics of a cylinder and the surface wave. Wei & Hu (2014) experimentally investigated the three-dimensional (3-D) effect on water entry with an impacting horizontal circular cylinder. Lyu *et al.* (2015) experimentally studied the water entry of a horizontal circular cylinder into flowing water with an impact velocity. The horizontal displacement was found to increase as the water velocity increases, and the trajectories of the hollow cylinder collapsed at the initial stage of submerging in water when the ratio of impact velocity to water velocity was the same as the solid cylinder. When the impact speed is relatively high, Wagner's (1932) theoretical framework can be used to study the impacting dynamical behaviour. For the liquid entry of an arbitrary 2-D body, Zhao & Faltinsen (1993) presented a simple asymptotic solution based on the Wagner theory, without considering the surface tension effect. Korobkin (1997) used the method of matched asymptotic expansions to analyse the high-speed liquid–solid impact problem while the role of the surface tension can be estimated by this method.

Some numerical research about a 2-D body or horizontal long cylinder falling or impacting onto water was also conducted. Zhu, Faltinsen & Hu (2007) numerically simulated the deformations of water surface induced by the water entry and exit of a horizontal 2-D circular cylinder with both forced and free vertical motions, and the simulated results were found to be in favourable agreement with the experimental results by Greenhow & Lin (1983). Hafsia *et al.* (2009) conducted a 2-D numerical simulation of a horizontal cylinder entering into and pulled out from water and well predicted the deformation of the interface as simulated by Lin (2007). Liu, Gao & Ding (2017) conducted 2-D modelling and simulations of fluid–structure interaction involving dynamic wetting as a horizontal circular cylinder sinks through the interface. Kiara, Paredes & Yue (2017) carried out a 2-D numerical investigation of the water entry of horizontal cylinders without and with spin. Iranmanesh & Passandideh-Fard (2017) performed 3-D numerical simulations on the water entry of a horizontal circular cylinder for low Froude numbers,

and the numerical results were found to be in a good agreement with the experimental data by Wei & Hu (2014).

Up to date, the work about the occurrence or non-occurrence of the resurrection (observed for an impacting superhydrophobic sphere; see Galeano-Rios *et al.* 2021) for a small cylinder impacting onto a liquid bath has not been reported. In this situation, some intriguing questions have been raised. Will the interesting resurrection occur for a small 2-D cylinder impacting onto a liquid bath? What are the ranges of the density of the impacting cylinder, the impact velocity, and the surface tension coefficient for the occurrence of the resurrection? What are the occurring mechanism and condition of the resurrection? Without doubt, these questions are crucial to the research about the impacting of small particles onto a liquid bath and the related industry.

In this paper, in order to answer the questions well, the impact of a small superhydrophobic cylinder onto a liquid bath is investigated using DNS based on the pseudo-solid method. The dynamic modes of the cylinder are studied and classified into four types. Various states of the impacting cylinder are comprehensively identified in a space of two parameters (the density ratio of the cylinder to the liquid and the Weber number). The occurring mechanism and condition of the resurrection are investigated.

2. Problem formation and mathematical methods

Figure 1 shows a schematic of a 2-D superhydrophobic circular cylinder of diameter D impacting downwards onto a liquid bath from air in a computational domain (spanning $10D$ in width and $20D$ in length) in a downward gravity field in Cartesian coordinates (\bar{x}, \bar{y}) . The initial cylinder velocity of non-zero magnitude is V (when the cylinder contacts the undisturbed liquid–gas surface), which is chosen as the reference velocity for our system. The related physical parameters used in our 2-D simulations can be found in table 1. To simplify the simulation of the fluid–solid interaction, the pseudo-solid approach is adopted (see the details in Appendix A), which has been shown as a satisfactory model for the impact of a solid sphere with a very large contact angle (Galeano-Rios *et al.* 2021). Within the pseudo-solid approach, a special stiff 2-D droplet with high viscosity (restricting the liquid motion inside) and high surface tension coefficient (restricting the relatively large deformation during impact) is used to simulate the solid cylinder. In our 2-D calculations, the densities of the pseudo-solid, the liquid and the gas are denoted by ρ_s , ρ_l and ρ_g , respectively, while the dynamic viscosities of the pseudo-solid, the liquid and the gas are denoted by μ_s , μ_l and μ_g , respectively. The surface tension coefficients of the pseudo-solid surface and the liquid surface are denoted by σ_s and σ_l , respectively. The dynamic viscosity of the pseudo-solid (i.e. the cylinder) is 250 times as large as that of the liquid in the bath (see μ_s/μ_l in table 1), while the surface tension coefficient of the pseudo-solid surface is 150 times as large as that between the liquid and the gas (see σ_s/σ_l in table 1).

Within the pseudo-solid method, it is unable to impose a value for the contact angle of the pseudo-solid. Instead, the contact angle of the pseudo-solid remains 180° naturally, due to the specific relation among the surface tensions of the solid–liquid, solid–gas and liquid–gas interfaces (see the details in Appendix A). Applying the pseudo-solid method, we find that there is a very thin film of gas with the thickness of approximately three meshes (less than $D/100$) between the pseudo-solid and the liquid and there is no triple contact line (CL; contact point in two dimensions) on the pseudo-solid. However, the liquid-entry behaviour with the superhydrophobic surface appears to be little influenced by

Resurrection of a superhydrophobic cylinder

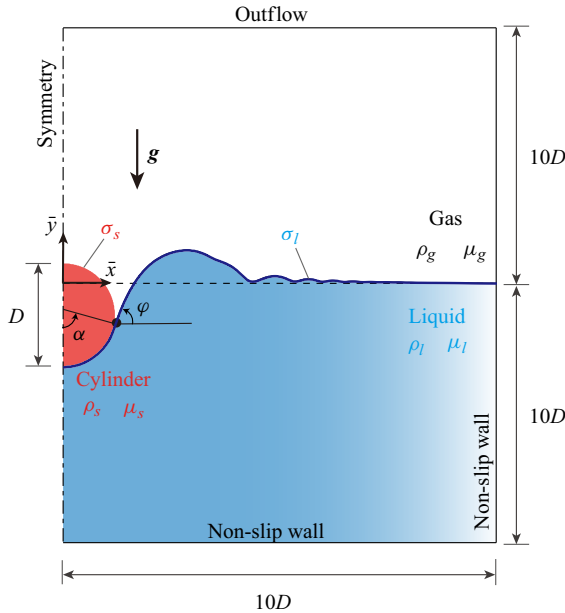


Figure 1. Schematic of a superhydrophobic circular cylinder impacting on the liquid surface. The origin of the dimensional Cartesian coordinates system (\bar{x}, \bar{y}) is located at the intersection of the symmetry axis (the vertical dot-dashed line) and the undisturbed liquid–gas interface (the horizontal dashed line). The azimuth angle α of the contact point (contact point in two dimensions) starting from the negative \bar{y} axis is equal to the inclination angle φ of the liquid surface at the contact line starting from the positive \bar{x} axis, because the theoretical contact angle θ is equal to 180° in the simulations (see [Appendix A](#)). Here α and φ are both measured counterclockwise.

Parameter	Symbol	Definition	Value
Surface tension coefficient ratio	—	σ_s/σ_l	150
Density ratio of gas to liquid	—	ρ_g/ρ_l	10^{-2}
Density ratio of pseudo-solid to liquid	λ_ρ	ρ_s/ρ_l	1–1.5
Viscosity ratio of gas to liquid	—	μ_g/μ_l	10^{-2}
Viscosity ratio of pseudo-solid to liquid	—	μ_s/μ_l	250
Reynolds number	Re	$\rho DV/\mu$	—
Reynolds number for the liquid	Re_l	$\rho_l DV/\mu_l$	2167.52
Weber number	We	$\rho DV^2/\sigma$	—
Weber number for the liquid	We_l	$\rho_l DV^2/\sigma_l$	5–80
Froude number	Fr	$V/(gD)^{1/2}$	5.60
Contact angle of the cylinder	θ	—	180°

Table 1. Values of relevant parameters used in our DNS.

the microscopic details of the contact with this surface, according to Galeano-Rios *et al.* (2021). We have explained this from the perspective of energy in [Appendix B](#).

The physical parameters are non-dimensionalised as follows:

$$x = \bar{x}/D, \quad y = \bar{y}/D, \quad u = \bar{u}/V, \quad v = \bar{v}/V, \quad v_s = \bar{v}_s/V, \quad \tau = tV/D, \quad (2.1a-f)$$

where u and v are the dimensionless horizontal and vertical velocities of the fluid, respectively, v_s is the dimensionless vertical velocity of the cylinder mass centre, and τ is the dimensionless time. The governing Navier–Stokes equations in dimensionless form

are given by

$$\nabla \cdot \mathbf{u} = 0, \tag{2.2}$$

$$\frac{\partial \mathbf{u}}{\partial \tau} + \mathbf{u} \cdot \nabla \mathbf{u} = -\nabla p + \frac{1}{Re} \nabla^2 \mathbf{u} + \frac{1}{We} \kappa \delta \mathbf{n} + \frac{1}{Fr^2}, \tag{2.3}$$

where the definitions of the dimensionless numbers Re , We and Fr are listed in [table 1](#), the Nabla operator $\nabla = (\partial/\partial x, \partial/\partial y)$, the velocity vector $\mathbf{u} = (u, v)$, κ denotes the curvature of the liquid–gas interface (the liquid surface) or the pseudo-solid surface, \mathbf{n} denotes the unit normal of the interface and δ denotes the Dirac delta function at the interface. The Bond number Bo (with $Bo = \rho g D^2 / \sigma$) is commonly employed for interfacial floatation ([Vella 2015](#)). To employ the Bond number in this paper is also feasible with the relationship $Bo = We / Fr^2$. To simplify our analysis, the Froude number Fr is set as a moderate constant ([table 1](#)), under which the highlighted resurrection is likely to occur. By changing We , the relative importance of the gravity and the surface tension (measured by Bo) varies. Thus, for the liquid-entry problem in this paper (with Fr fixed), there is no essential difference between using Bo and using We .

To mark the interface location, the volume fraction functions $c_l(x, y, t)$ and $c_s(x, y, t)$ are used, with which the value of c_l , c_s and $1 - c_l - c_s$ denote the volume fraction of the liquid, the pseudo-solid and the gas, respectively, in a computational cell. The domains of $c_l = 1$, $c_l = 0$ and $0 < c_l < 1$ represent the liquid, the gas and the liquid surface, respectively, while the domains of $c_s = 1$, $c_s = 0$ and $0 < c_s < 1$ represent the pseudo-solid, the liquid or gas and the pseudo solid surface, respectively. The volume fractions c_l and c_s are governed by the advection equations:

$$\frac{\partial c_l}{\partial \tau} + \nabla \cdot (c_l \mathbf{u}) = 0, \tag{2.4}$$

$$\frac{\partial c_s}{\partial \tau} + \nabla \cdot (c_s \mathbf{u}) = 0. \tag{2.5}$$

For the whole computational domain, the density ρ (dynamic viscosity μ) can be interpolated with the pseudo-solid density ρ_s (dynamic viscosity μ_s), the liquid density ρ_l (dynamic viscosity μ_l) and the gas density ρ_g (dynamic viscosity μ_g):

$$\rho = \rho_s c_s + \rho_l c_l + \rho_g (1 - c_s - c_l), \tag{2.6}$$

$$\mu = \mu_s c_s + \mu_l c_l + \mu_g (1 - c_s - c_l). \tag{2.7}$$

To reduce computational cost, the symmetry boundary condition is set at the left side of the computational domain. Only the right half of the physical domain will be computed (see [figure 1](#)). In addition, the outflow boundary condition is employed at the top of computational domain as

$$\frac{\partial u}{\partial y} = \frac{\partial v}{\partial y} = 0, \tag{2.8}$$

while no-slip boundary conditions are employed at the right side and the bottom of the computational domain as

$$u = v = 0. \tag{2.9}$$

The DNS are implemented using the well-known, open-source, volume-of-fluid (VoF) package Gerris ([Popinet 2003, 2009](#)). The adaptive mesh refinement is adopted and the local mesh sizes are adjusted depending on the interfacial location, the velocity gradient and the vorticity. An independence analysis is conducted to determine the appropriate domain size and grid refinement (see [Appendix C](#)).

Resurrection of a superhydrophobic cylinder

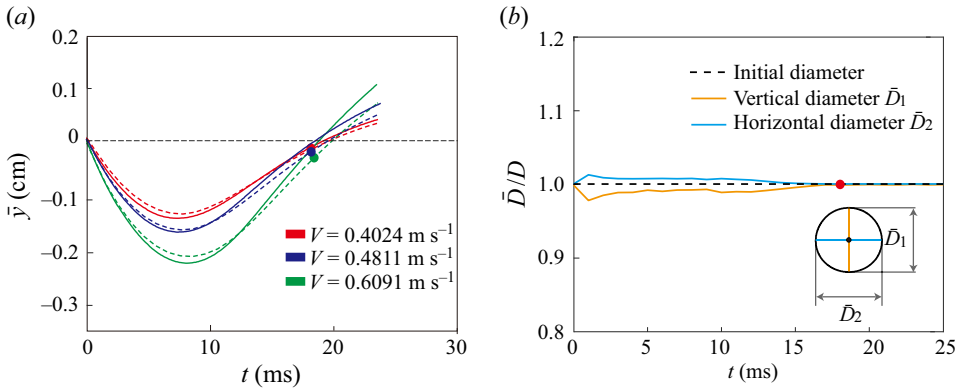


Figure 2. (a) Trajectory of the lowest point on the sphere. Solid curves correspond to experimental data by Galeano-Rios *et al.* (2021) and dashed curves to our 2-D axisymmetric simulations. The circle points indicate the moment when the sphere gets detached from the water surface in our simulations. (b) Time evolution of pseudo-solid deformation in our simulation. The data in (b) correspond to the simulation of $V = 0.4024 \text{ m s}^{-1}$ in (a). The deformed diameters \bar{D}_1 and \bar{D}_2 are as defined in the inset of (b). For the liquid (i.e. water), the parameters are given as density $\rho_l = 10^3 \text{ kg m}^{-3}$, viscosity $\mu_l = 0.978 \times 10^{-3} \text{ Pa s}$ and the surface tension of the liquid surface $\sigma_l = 0.072 \text{ N m}^{-1}$. For the solid sphere (pseudo-solid in simulations), the parameters are given as initial diameter $D = 0.166 \text{ cm}$, density $\rho_s = 2.2 \times 10^3 \text{ kg m}^{-3}$, viscosity $\mu_s = 250 \mu_l$ and the surface tension of the pseudo-solid surface $\sigma_s = 20 \sigma_l$. These values of parameters are also seen in Galeano-Rios *et al.* (2021). For the parameters of gas (not given in Galeano-Rios *et al.* (2021)), $\rho_g = 10 \text{ kg m}^{-3}$ and $\mu_g = 10^{-5} \text{ Pa s}$ are employed in our simulations.

3. Results and discussion

In order to show the validity of our DNS results, we simulate the impact of a superhydrophobic sphere onto a liquid bath using the 2-D axisymmetric model and compare the calculated results at different times with the experimental data by Galeano-Rios *et al.* (2021), as shown in figure 2. The parameters of liquid and solid in Galeano-Rios *et al.* (2021) are employed in these simulations while the parameters of gas in theirs are not given. We employ $\rho_g = 10 \text{ kg m}^{-3}$ (with $\rho_g/\rho_l = 10^{-2}$) and $\mu_g = 10^{-5} \text{ Pa s}$ for the gas in these simulations. The gas–liquid density ratio of $\rho_g/\rho_l = 10^{-2}$ is larger than that in reality (approximately 10^{-3}) while the influence of gas is still negligible. In addition, we find the density ratio of $\rho_g/\rho_l = 10^{-2}$ (also in table 1) can possibly tune the Gerris solver for better convergence. The numerical results are in a good agreement with the published experimental data. Notably, the equilibrium contact angle of the sphere is 160° for the experiments in Galeano-Rios *et al.* (2021) while the contact angle in our simulations is naturally 180° , which may account for the error of our simulations in figure 2(a). In addition, the deformation of the pseudo-solid used to simulate the sphere is generally less than 5 % of the original sphere diameter, as shown in figure 2(b). This proves validity and applicability of the pseudo-solid approach used here, as it was in Galeano-Rios *et al.* (2021). It should be noted that surface tension and viscosity of the pseudo-solid for the 2-D axisymmetric model are adopted from Galeano-Rios *et al.* (2021). For the 2-D cases focused on in this paper, the pseudo-solid parameters (i.e. σ_s/σ_l and μ_s/μ_l in table 1) can also achieve the maximum deformation less than 5 % of the original cylinder diameter.

3.1. Four flow regimes

For the simplicity of our investigation, the Reynolds number for the liquid Re_l is fixed in the following (as in table 1). Four typical flow regimes are identified in our simulations. Flow

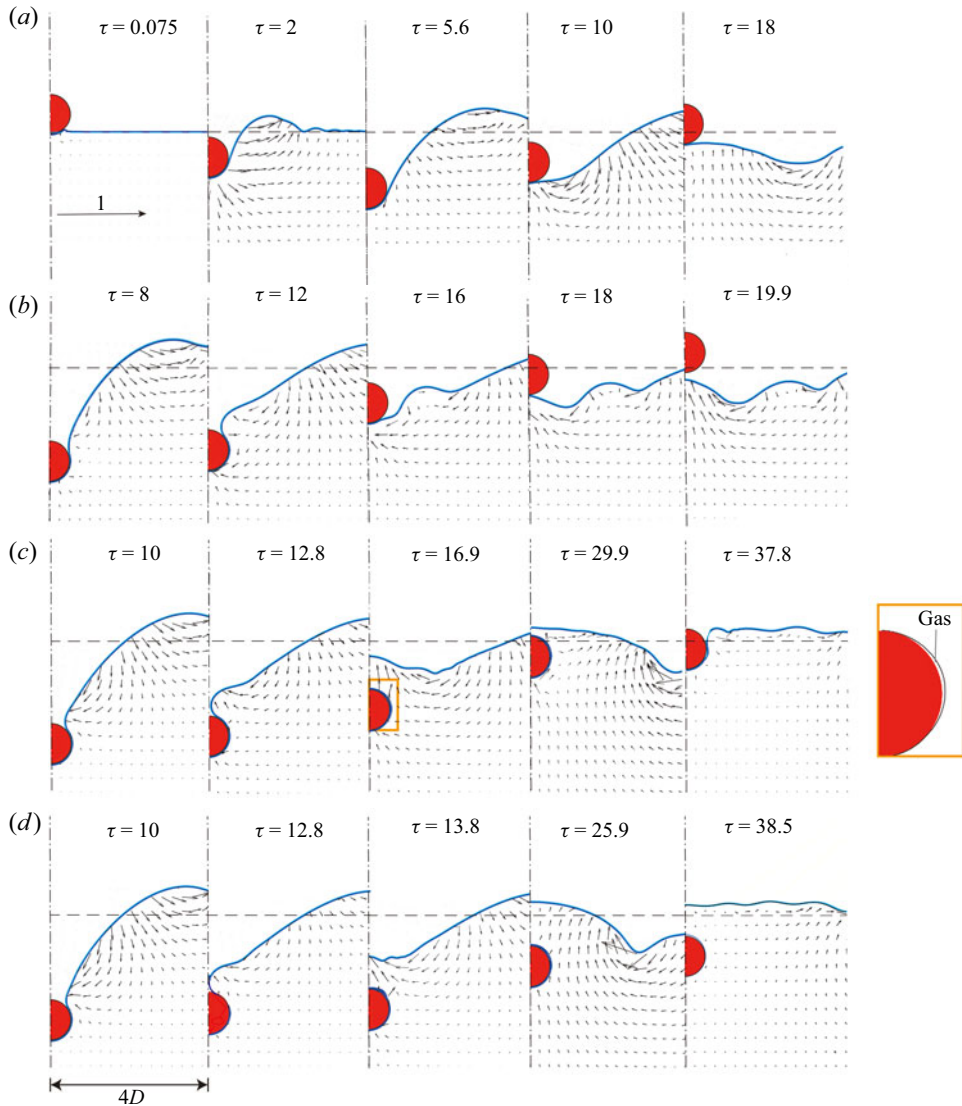


Figure 3. Representative snapshots of a superhydrophobic cylinder impacting on the liquid surface (where $\lambda_\rho = 1.2$ and $\theta = 180^\circ$) for four distinct impact regimes: (a) floating for $We_l = 15$, (b) bouncing for $We_l = 30$, (c) resurfecting for $We_l = 37$ and (d) sinking for $We_l = 40$. The blue curves denote the gas–liquid interfaces, and the black arrows denote the velocity vectors. The width for the domain depicted in each snapshot is $4D$ (see the first snapshot in *d*) and the scale is uniform in length and width. The enlarged drawing at the right in this figure corresponds to the snapshot of $\tau = 16.9$ in *(c)*, where gas is trapped around the cylinder.

characteristics (including the interface evolution and the liquid velocity vector) of the four are shown in figure 3. For a given density ratio λ_ρ , the four regimes (floating, bouncing, resurfecting and sinking) appear in sequence as the liquid Weber number We_l (which is more representative than the Weber number for the gas or pseudo-solid) increases. For the different regimes in figure 3, the corresponding mass centre location and velocity of the cylinder are shown in figure 4(a,b), respectively. An interesting observation can be made for the highlighted case of resurfecting (see figure 3(c) and the green dot-dashed line in figure 4(a)). When the cylinder reaches the lowest position (with the minimum value of y),

Resurrection of a superhydrophobic cylinder

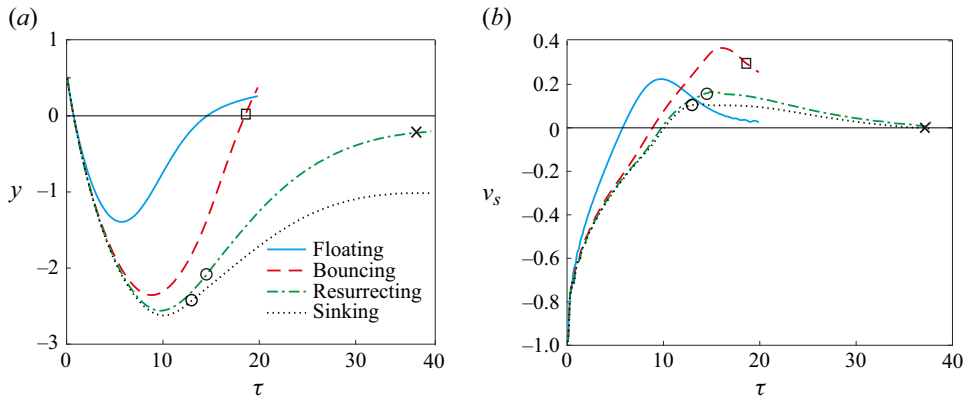


Figure 4. Time evolution of (a) centre height and (b) vertical velocity of the cylinder centre for the four flow regimes in figure 3, i.e. floating ($We_l = 15$), bouncing ($We_l = 30$), resurrecting ($We_l = 37$) and sinking ($We_l = 40$). The black solid line of $y = 0$ indicates the undisturbed liquid line height, (\square) indicates the moment when the cylinder starts to detach from the liquid, (\circ) represents the moment when the cylinder is just fully submerged by liquid and (\times) indicates the moment when the cylinder starts to resurface from the liquid.

the cylinder is not yet fully immersed and the surface tension still plays a role. The cylinder begins to ascend after passing the lowest position and then becomes fully immersed. It is founded that this interesting process typically accounts for approximately 10–15 % of the entire impact (from initial touch of $\tau = 0$ to the moment of resurfacing, see the cross in figure 4).

For the floating regime (in figure 3a), the cylinder remains descending after coming into contact with the liquid, and then starts to ascend at the lowest position (see the image of $\tau = 5.6$ in figure 3a) due to the recovery of the liquid–gas interface. Meanwhile, the cylinder remains attached to the liquid–gas interface. For the bouncing regime (in figure 3b), the cylinder movement is similar to that of the floating regime, except that the cylinder separates from the liquid during the ascent motion (see the image of $\tau = 19.9$ in figure 3b). For the resurrecting regime (in figure 3c), the cylinder also undergoes a descent motion and then an ascent motion. During the ascent motion, the air cavity pinches off and the cylinder is fully submerged (see the image of $\tau = 12.8$ in figure 3c). However, the cylinder will finally break through the interface (see the image of $\tau = 37.8$ in figure 3c). For the sinking regime (in figure 3d), the cylinder will never break through the interface after fully submerged.

Figure 5 shows the phase diagram of the flow regimes for a cylinder impacting on the liquid surface in a parameter space (λ_ρ , We_l). Only the cases of $\lambda_\rho \geq 1$ are considered, because the cylinder with its density smaller than the liquid density ($\lambda_\rho < 1$) will manifest itself eventually even if the impacting velocity is extremely high. When the density of the cylinder is slightly smaller than that of the liquid, the impacting cylinder can become fully immersed at first while it may take a significant time for the cylinder to resurface, depending on the impact velocity V . For a specific density ratio λ_ρ , as We_l increases from 0 to a large enough value, the four regimes, i.e. floating, bouncing, resurrecting and sinking, appear sequentially. It can be seen from figure 5 that the resurrection occurs in a very narrow region (between the solid curve and the dot-dashed curve). For a large enough density ratio λ_ρ (larger than 1.3 or so), the resurrection will never occur.

In most cases of the resurrecting regime, we find that the cylinder will remain afloat after resurfacing (see figure 3(c) and black crosses in figure 5). Meanwhile, in very rare cases of

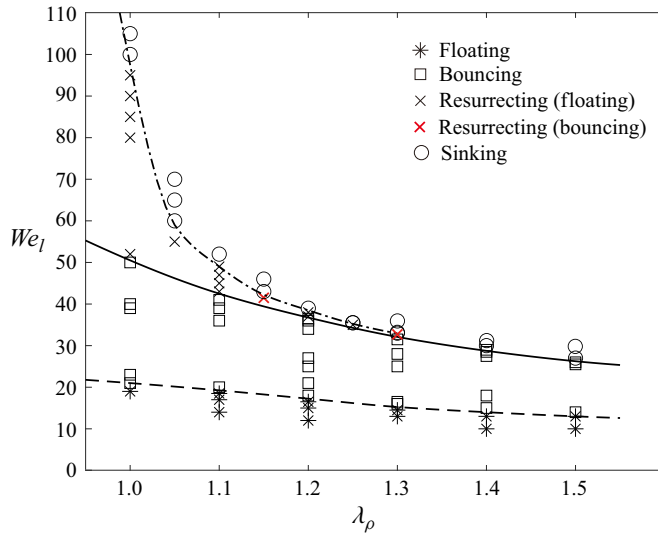


Figure 5. Phase diagram of a 2-D cylinder impacting onto a liquid bath in a parameter space (λ_ρ , We_l). The four phases include the regimes of floating, bouncing, resurrecting (with floating and bouncing) and sinking. The cases of resurrecting with bouncing are rare for the impacting cylinder. Other parameters are listed in table 1.

the resurrecting regime, the cylinder will bounce and get detached from the liquid surface after resurfacing (denoted by red crosses in figure 5). However, for the superhydrophobic sphere impacting onto the liquid, the regime of resurrecting with bouncing has been found (see figure 11 in Galeano-Rios *et al.* 2021) but the regime of resurrecting with floating has not been found so far. Though the cases of resurrecting (with bouncing or floating) are rare for both the impacting cylinder and the impacting sphere, the resurrection with floating seems more possible to occur for the cylinder while the resurrection with bouncing seems more possible to occur for the sphere.

An interesting result can be found in figure 5 that the large density ratio λ_ρ is helpful to the occurrence of bouncing rather than floating for the impacting cylinder (at a given value of We_l , e.g. $We_l = 20$). A similar result can also be seen in figure 7 of Lee & Kim (2008). Only the cases of bouncing and floating are considered here. When the superhydrophobic cylinder descends at the beginning, its mechanical energy is absorbed by the liquid. After the cylinder reaches the lowest point, the surface tension force lifts the superhydrophobic cylinder up and the energy returns to the cylinder (with a dissipation of the energy). Similar to the cases of the impacting sphere (Galeano-Rios *et al.* 2021), the cylinder with higher density (larger value of λ_ρ) recovers relatively more energy during impact than the cylinder with lower density. Thus, the large density ratio λ_ρ promotes the occurrence of bouncing.

3.2. Force analysis

For the force analysis of the cylinder, we use the dimensional forms for all physical quantities to aid in the comprehension. During the impact, the forces acting on the cylinder are the capillary force, the gravitational force and the hydrodynamic force. The hydrodynamic force can be regarded as the sum of the form drag, the hydrostatic pressure and the added inertia force.

Though there is no microscopic three-phase CL (point) in our simulations with the pseudo-solid approach (due to the very thin gas film between the solid and the liquid),

Resurrection of a superhydrophobic cylinder

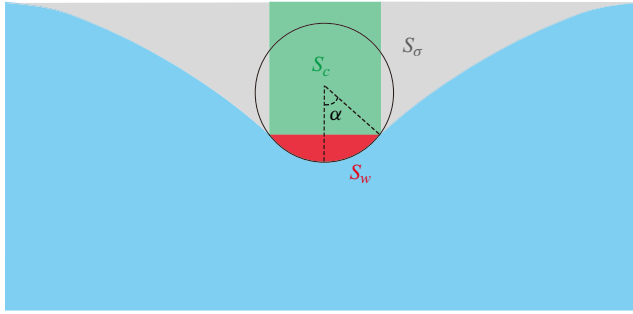


Figure 6. The volumes of liquid displaced by the wetted portion of the cylinder (S_w), the deformed liquid–gas interface (S_σ) and the cavity above the wetted portion of the cylinder (S_c).

the interface configurations in our simulations are relatively accurate because of the same essence in surface energies (see [Appendix B](#)). To analyse the forces on the cylinder theoretically, the position of the CL is estimated based on the configurations from the simulations. The position on the cylinder where the thickness of the thin gas film rapidly increases (i.e. the end of the thin gas film) is deemed as the contact point.

From the Newton's second law, the motion of the cylinder can be described as

$$(m_s + m_a) \frac{d\bar{v}_s}{dt} = \bar{f}_p + \bar{f}_d + \bar{f}_\sigma + \bar{f}_G, \quad (3.1)$$

where the mass of the cylinder is given by $m_s = \pi D^2 \rho_s / 4$ and m_a denotes the added mass. Here $\bar{f}_p, \bar{f}_d, \bar{f}_\sigma$ and \bar{f}_G are the vertical components of the hydrostatic pressure force, the form drag force, the surface tension force and the gravitational force, respectively. The vertical component of the hydrostatic pressure force \bar{f}_p is equal to the total weight of liquid displaced by the wetted portion of the cylinder and the cavity above the wetted portion of the cylinder. Following Vella & Li (2010) and Bush & Hu (2006), the vertical component of the hydrostatic pressure force can be expressed as

$$\bar{f}_p = [S_w + S_c] \rho_l g, \quad (3.2)$$

where $S_w = (\alpha - \sin \alpha \cos \alpha) \rho_l D^2 / 4$ is the volume of liquid displaced by the wetted portion of the cylinder, $S_c = \rho_l D \sin \alpha (-h + (D/2) \cos \alpha)$ is volume of liquid displaced by the cavity above the wetted portion of the cylinder (see [figure 6](#)) and h is the vertical coordinate of the cylinder centre. The other three force components can be expressed as

$$\bar{f}_d = -\frac{1}{2} C_d \rho_l D |\bar{v}_s| \bar{v}_s, \quad \bar{f}_\sigma = 2\sigma \sin \varphi, \quad \bar{f}_G = -m_s g, \quad (3.3a-c)$$

where C_d denotes the drag coefficient. The added mass m_a denotes the mass of liquid displaced by the wetted portion of the cylinder (where $m_a = \rho_l S_w$). With (3.2) and (3.3a-c), we can rewrite (3.1) as

$$\left(\rho_s \pi \frac{D^2}{4} + \rho_l S_c \right) \frac{d\bar{v}_s}{dt} = [S_c + S_w] \rho_l g + \frac{1}{2} C_d \rho_l D \bar{v}_s^2 + 2\sigma \sin \varphi - m_s g. \quad (3.4)$$

For the cases of medium We_l in this paper, the impact process in each flow regime can be divided into three stages: slamming, pinning and sliding. [Figure 7\(a\)](#) shows the time evolution of the vertical components of the hydrodynamic force, the capillary force and the gravitational force exerted on the cylinder for the three stages. In [figure 7\(b\)](#), $\sin \alpha$

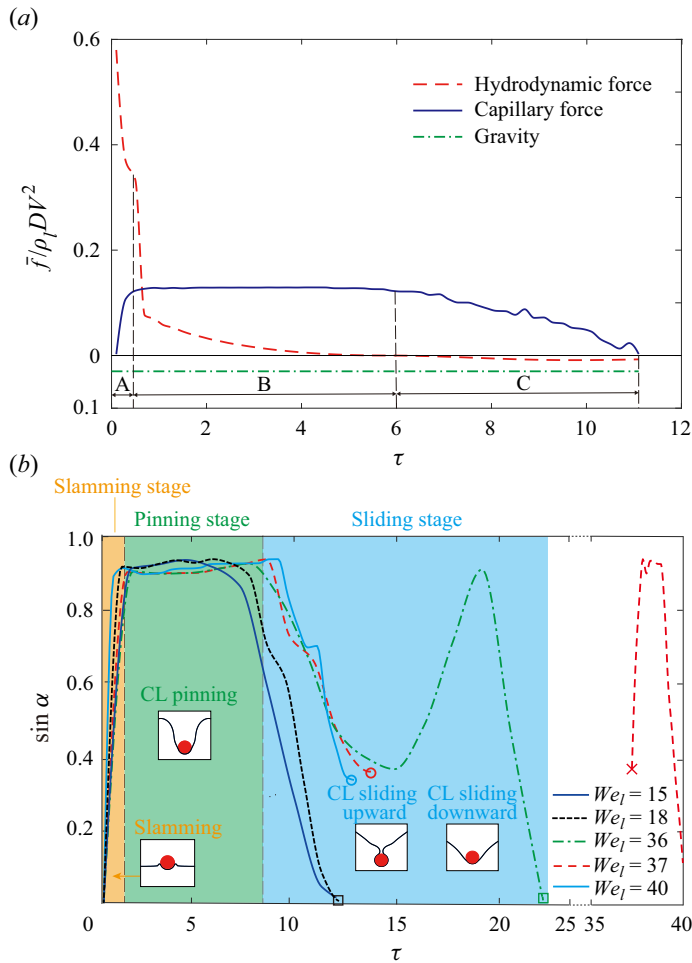


Figure 7. Time evolution of (a) vertical components of the total hydrodynamic force, the capillary force and the gravitational force exerted on the cylinder for the case of floating regime at $We_l = 15$ and $\lambda_\rho = 1.2$, and (b) strength of the vertical component of the capillary force in terms of $\sin \alpha$ at $\lambda_\rho = 1.2$ for $We_l = 15$ (floating), $We_l = 18$ (bouncing), $We_l = 36$ (bouncing), $We_l = 37$ (resurrecting) and $We_l = 40$ (sinking). In (a), time ranges A, B and C correspond to the slamming, pinning and sliding stages, respectively. In (b), (\square) indicates the moment when the cylinder starts to detach from the liquid, (\circ) represents the moment when the cylinder is just fully submerged by liquid and (\times) indicates the moment when the cylinder starts to resurface from the liquid. The snapshots in the four insets of (b) correspond to $\tau = 0.4, 5, 13$ and 19.5 (from left to right) for $We_l = 36$. For $We_l = 15, 37$ and 40 , the corresponding snapshots are seen in figure 3.

can indicate the position of the CL and the magnitude of the vertical capillary effect. The slamming stage is the early period of impact process, at which the cylinder velocity decreases rapidly due to the hydrodynamic force. The CL rapidly climbs to the cylinder surface of $\alpha \approx 90^\circ$, where the vertical component of the capillary force reaches almost its maximum value. In this stage, the movement of the cylinder is dominated by the hydrodynamic force. After climbing to the cylinder surface of $\alpha \approx 90^\circ$, the CL is pinned at this position, and the pinning stage starts. The capillary force remains nearly constant due to pinning (see figure 7a) and the hydrodynamic force decreases slowly from a relatively low value. At this pinning stage, the most dominant force is the capillary force.

Resurrection of a superhydrophobic cylinder

At the end of the pinning stage, the downward velocity of the cylinder further decreases to approximately zero. At the sliding stage, the cylinder begins to ascend under the effect of the capillary force. For a relatively small We_l (in the floating regime), the CL begins to slide downward from the pinned position (i.e. α decreases from 90° , see [figure 3a](#)). Meanwhile, for a relatively large We_l (in the resurrecting or sinking regime), the CL begins to slide upward from the pinned position (i.e. α increases from 90° , see [figure 3c,d](#)). In the bouncing regime, the CL may slide downwards continuously from the pinned position before the cylinder becomes detached from the liquid (e.g. $We_l = 18$ in [figure 7b](#)), or the CL will slide upwards from the pinned position and then slide downwards continuously before the detachment (e.g. $We_l = 36$ in [figure 7\(b\)](#), see the corresponding insets).

3.3. Early stage motion analysis

In this section, we present a simplified model to predict the early-stage motion of an impacting cylinder for the cases in the regime of floating and the regime of bouncing according to the above force analysis.

At the slamming stage, the hydrodynamic force is dominant. From Ji, Song & Yao (2017), the magnitude of the hydrostatic pressure force is much smaller than the form drag and the added inertia force. The hydrostatic pressure force can be neglected throughout this stage. Due to the relatively high velocity of the cylinder during this stage ($We_l > 5$ in this paper), the form drag is significantly greater than other forces. Therefore, we only consider the form drag at this stage, and (3.4) can be rewritten as

$$\frac{d\bar{v}_s}{dt} = \frac{2C_d\rho_l}{\rho_s\pi D}\bar{v}_s^2. \quad (3.5)$$

Integrating (3.5) with the initial condition $\bar{v}_s = -V$, we can obtain the cylinder velocity as a function of the time at the slamming stage:

$$\bar{v}_s = -\frac{\pi D\lambda_\rho}{2C_d t + \pi D\lambda_\rho V^{-1}}. \quad (3.6)$$

Previous studies on the drag coefficient of a partially immersed superhydrophobic cylinder remain inadequate. The experiments in Hunt *et al.* (2023) indicate that the drag coefficient is 0–1.5 for a partially immersed superhydrophobic sphere, depending on the impacting velocity, the diameter and the vertical position. When fully immersed, the drag coefficient of the cylinder is approximately double that of the sphere with the same diameter for $Re \sim 10^3$ (White 2016). Taking these into account, we find that the value of 1.5 can be appropriate for C_d at the slamming stage in the cases of this paper.

At the pinning stage of the cylinder, the capillary force starts to play a role and its vertical component can be seen as a constant (see [figure 7a](#)). In the meantime, the form drag and the added inertia force also play roles, because the cylinder velocity is still large enough at the whole stage. The volume of liquid displaced by cylinder is equal to half the volume of the cylinder, leading to $\alpha \approx 90^\circ$ or $\sin \alpha \approx 1$ (see [figure 7b](#)). The gravity force is also taken into consideration. At this stage, (3.4) is therefore reduced to

$$\left(\rho_s + \frac{1}{2}\rho_l\right)\pi\frac{D^2}{4}\frac{d\bar{v}_s}{dt} = \frac{1}{2}C_d\rho_l D\bar{v}_s^2 + 2\sigma + \rho_s\pi\frac{D^2}{4}g. \quad (3.7)$$

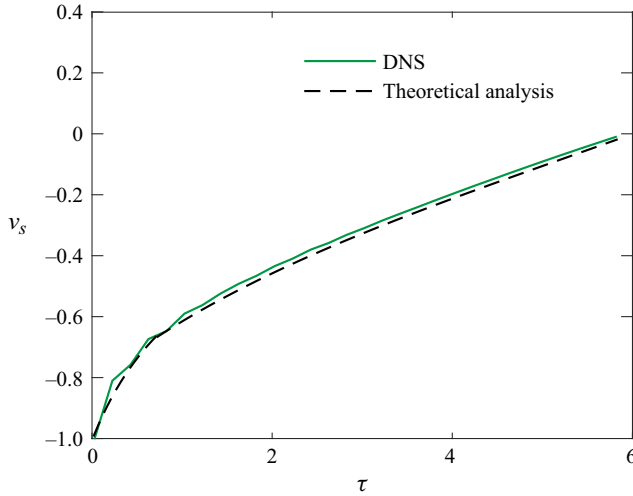


Figure 8. Time evolution of the non-dimensional cylinder velocity v_s (where $v_{cr} = \bar{v}_{cr}/V$) at the slamming stage and the pinning stage for a case of the floating regime at $We_l = 15$ and $\lambda_\rho = 1.2$. The dashed curve denotes theoretical results that are calculated from (3.6) and (3.8).

Integrating (3.7), we can obtain the time evolution of the cylinder velocity at the pinning stage:

$$\bar{v}_s = -\sqrt{\frac{8\sigma + \lambda_\rho \rho_l D^2 g}{2C_d \rho_l D}} \tan\left(-\sqrt{2C_d D \rho_l (8\sigma + \lambda_\rho \rho_l D^2 g)} \frac{2t}{\rho_l \pi D^2 (1 + 2\lambda_\rho)} + C\right), \quad (3.8)$$

where C denotes a parameter to be determined.

Figure 8 shows the DNS result of the cylinder velocity for the case of figure 3(a), which is also compared with the theoretical prediction of (3.6) and (3.8). For this case, when $\tau = tV/D \approx 0.7$, which corresponds to the start of the pinning stage, the cylinder velocity is given by $v_s = \bar{v}_s/V = -0.68$. Accordingly, we can obtain the parameter $C = 0.846$ in (3.8). For the drag coefficient of the partial immersed body at the pinning stage, we use $C_d = 0.6$ (in Vella & Li (2010), $C_d = 0.6$ was also used in a similar case) in theoretical calculations.

3.4. Critical condition for resurrection

As shown in figure 5, the transition between the resurrecting regime and the sinking regime only exists for $\lambda_\rho \leq 1.3$. From figure 3(c,d), the cylinder will be completely submerged after the cavity above the cylinder pinches off. Then the cylinder continues to accelerate upward under the inertial propulsion of the surrounding fluid for a short time. Subsequently, the cylinder starts to decelerate due to the drag of the surrounding fluid. During the decelerating process, the forces acting on the cylinder are the buoyancy force, the form drag, the gravitational force and the added inertia force. Therefore, following Kim *et al.* (2015), the motion of the fully immersed cylinder can be expressed as

$$(m_s + m_a) \frac{d\bar{v}_s}{dt} = \bar{f}_b + \bar{f}_d + \bar{f}_G, \quad (3.9)$$

where $\bar{f}_b = \pi D^2 \rho_l g/4$. For the fully submerged cylinder moving perpendicular to the axis of itself, by substituting $\alpha = \pi$ into $m_a = (\alpha - \sin \alpha \cos \alpha) \rho_l D^2/4$, the added mass

Resurrection of a superhydrophobic cylinder

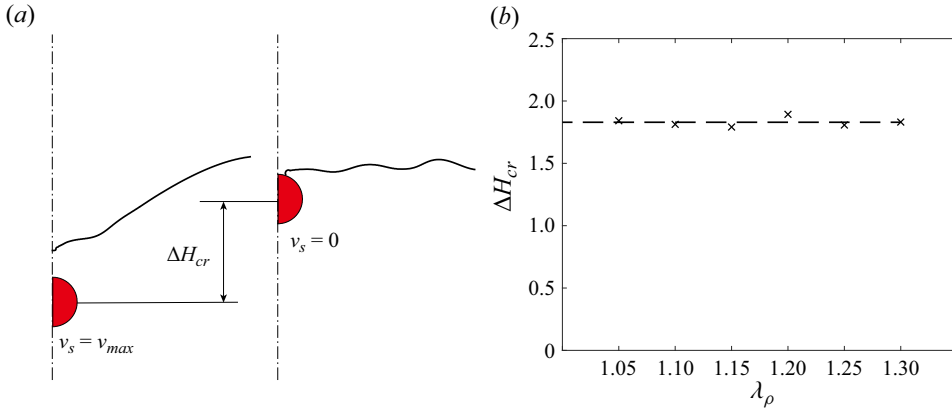


Figure 9. (a) The definition of the non-dimensional critical height difference, where $\Delta H_{cr} = \Delta \bar{H}_{cr}/D$. (b) ΔH_{cr} for different values of λ_ρ ; (x) indicate the results from DNS.

becomes $m_a = \pi D^2 \rho_l / 4$ (see also White 2016). The drag coefficient is given by $C_d \approx 1.5$, which is the appropriate value for a fully submerged cylinder (see Vella & Li 2010). Equation (3.9) can therefore be rewritten as

$$[(1 - \lambda_\rho)g] - \frac{2C_d \bar{v}_s^2}{\rho_l \pi D} = (\lambda_\rho + 1) \frac{d\bar{v}_s}{dt}. \quad (3.10)$$

We consider the critical cases that the cylinder velocity will precisely decelerate to zero at the moment when it breaks through the interface (see the cross in figure 4). At $t = t_s$, the cylinder just reaches its maximum upwards velocity \bar{v}_{cr} (see figure 9a). This velocity is critical for the regime of sinking and the regime of resurrecting. Solving the ordinary differential equation (3.10), it can be obtained that

$$\bar{v}_s = \sqrt{\frac{C_1}{C_2}} \tan[C_3 - \sqrt{C_1 C_2}(t - t_s)], \quad (3.11)$$

where

$$C_1 = \frac{(\lambda_\rho - 1)g}{\lambda_\rho + 1}, \quad C_2 = \frac{2C_d}{(\lambda_\rho + 1)\rho_l \pi D}, \quad C_3 = \arctan\left(\sqrt{\frac{C_2}{C_1}} \bar{v}_{cr}\right). \quad (3.12a-c)$$

For the case that is precisely at the transition between the resurrecting regime and the sinking regime, the cylinder velocity will precisely decelerate to zero at the moment when it breaks through the interface. By letting $\bar{v}_s = 0$ in (3.11), we can get the moment t_e when the cylinder just breaks through the interface. Integrating the velocity \bar{v}_s in (3.11) from $t = t_s$ to $t = t_e$, we can obtain

$$\Delta \bar{H}_{cr} = \frac{1}{2C_2} \ln\left(1 + \frac{C_2}{C_1} \bar{v}_{cr}^2\right), \quad (3.13)$$

where $\Delta \bar{H}_{cr}$ denotes the critical height difference between the point where the cylinder is just reaches its maximum upwards velocity v_{max} and the point where the cylinder just breaks through the interface (see figure 9a).

We find that the critical height difference $\Delta \bar{H}_{cr}$ almost remains constant for different density ratios, as is shown in figure 9(b). Notably, for a very large density ratio λ_ρ (larger

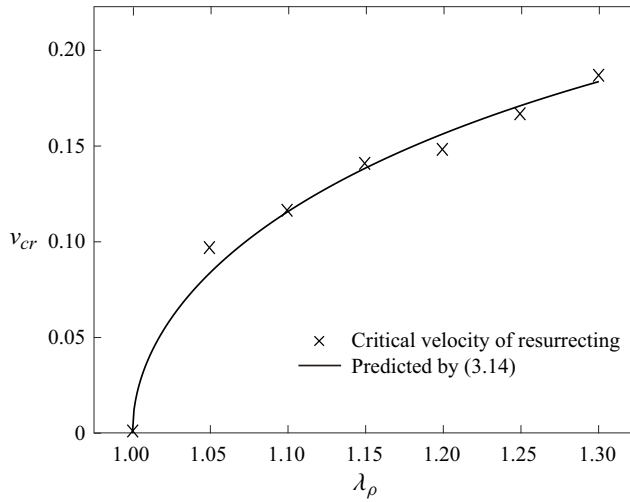


Figure 10. Non-dimensional critical velocity v_{cr} as a function of λ_ρ , where $v_{cr} = \bar{v}_{cr}/V$. All crosses are obtained from the cases in the resurrecting regime closest to the boundary between the resurrecting regime and the sinking regime in the phase diagram (figure 5), except for the cross at $\lambda_\rho = 1$, which is predicted theoretically.

than 1.3 in figure 5), the regime of resurrecting does not exist, leading no critical case. As depicted in figure 5, the allowable parameter region for resurrecting is relatively narrow for both λ_ρ and We_l , which may account for the constancy of the value of $\Delta\bar{H}_{cr}$. Thus, the critical velocity \bar{v}_{cr} of the fully immersed cylinder can be obtained from (3.13) as

$$\bar{v}_{cr} = \sqrt{\frac{C_1}{C_2}(e^{2C_2\Delta\bar{H}} - 1)}. \tag{3.14}$$

The critical velocity \bar{v}_{cr} for different λ_ρ calculated by (3.14) is compared with the corresponding DNS results, as shown in figure 10. During the whole entry, if the maximal velocity of the cylinder after fully immersed is larger than \bar{v}_{cr} , the resurrection will occur for the cylinder.

4. Conclusions

We have numerically investigated the impact of a superhydrophobic cylinder onto a liquid bath. The results demonstrate that with an increase in the Weber number, the system exhibits four distinct flow regimes, i.e. floating, bouncing, resurrecting and sinking regimes. The highlighted resurrecting regime pictures that, even if the cylinder is fully submerged in the liquid during the impact, it can still emerge from the liquid. With a further analysis, we find that when the cylinder reaches the lowest position, the cylinder is not fully immersed yet and the surface tension still plays a role. After reaching this position, the cylinder begins to move up when influenced by the surface tension force. Subsequently, the cylinder is fully immersed in the liquid and the surface tension effect on the cylinder disappears. For the resurrecting regime, the duration for the cylinder ascending from the lowest position to the full immersion position is approximately 10–15% of the entire process (from initial touching the liquid surface to resurfacing). The fully immersed cylinder then continues moving up and resurfaces eventually, even if its speed is slowed down by the viscous drag.

From further numerical results, the phase diagram for the four regimes is presented in a parameter space of the Weber number and the particle-to-liquid density ratio. The resurrection regime for the impacting cylinder can only exist at a relatively narrow parameter space (where the Weber number is medium and the cylinder density is not very large). A force analysis is conducted for the impacting cylinder, and three stages (i.e. slamming, pinning and sliding) can be divided according to the effect of the surface tension (or the CL position). We find that the form drag dominates in the slamming stage while the surface tension force and the gravity force also play roles in the pinning stage, which can be applied to analyse the early stage motion of an impacting cylinder.

In order to predict whether the interesting resurrection phenomenon will occur for the impacting cylinder, the dynamics is investigated for the cylinder when it is fully immersed. We find that the critical height for the cylinder to resurface is almost constant for different cylinder densities. With this finding, the critical velocity of the fully immersed cylinder is derived, which can be used for the prediction of resurrection.

Funding. This research was supported in part by the National Natural Science Foundation of China (no. 11972170).

Declaration of interests. The authors report no conflict of interest.

Author ORCID.

-  Wanqiu Zhang <https://orcid.org/0000-0003-0306-9030>;
-  Yaochen Mei <https://orcid.org/0009-0008-6269-1237>;
-  Xinping Zhou <https://orcid.org/0000-0001-6340-5273>.

Appendix A

To aid in the comprehension of the pseudo-solid approach, the volume fractions of liquid and solid (c_l and c_s) for the three phases are shown in figure 11. At the triple-phase region, the (surface tension) force balance can be expressed as

$$\sigma_{lg} \cos \varphi + \sigma_{sg} \cos \beta + \sigma_{sl} \cos \gamma = 0, \tag{A1a}$$

$$\sigma_{lg} \sin \varphi + \sigma_{sg} \sin \beta + \sigma_{sl} \sin \gamma = 0, \tag{A1b}$$

where σ_{lg} , σ_{sg} and σ_{sl} denote the surface tension coefficients for the liquid–gas interface, the solid–gas interface and the solid–liquid interface, respectively.

For the VoF method, the theoretical surface tension coefficient σ_l (σ_s), as presented in table 1, works in the domain where $0 < c_l < 1$ ($0 < c_s < 1$). Thus, we have $\sigma_{lg} = \sigma_l$ for the liquid–gas interface, while having $\sigma_{sg} = \sigma_s$ for the solid–gas interface. The two points meet our expectations. However, for the solid–liquid interface, both $0 < c_l < 1$ and $0 < c_s < 1$ are satisfied, leading to the relation that

$$\sigma_{sl} = \sigma_l + \sigma_s = \sigma_{lg} + \sigma_{sg}. \tag{A2}$$

Notably, the relation (A2) is deduced from the characteristic of the VoF method, instead of the physical fact. With (A1a,b) and (A2), we can obtain the angle relation:

$$\varphi = \beta, \quad \gamma = \varphi - \pi. \tag{A3a,b}$$

From (A3), it can be deduced that the contact angle θ is fixed, given by

$$\theta = \varphi - \gamma = \pi. \tag{A4}$$

The theoretical contact angle for the pseudo-solid approach is 180° , which accounts for the agreement with the superhydrophobic cases.

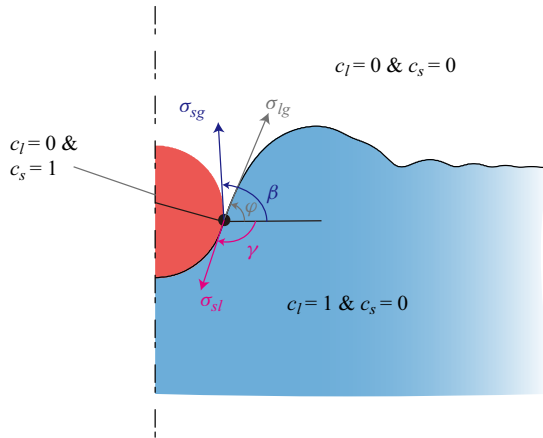


Figure 11. Surface tension forces at the three-phase region. The surface tension coefficients for the liquid–gas interface, the solid–gas interface and the solid–liquid interface are denoted by σ_{lg} , σ_{sg} and σ_{sl} , respectively. The direction angles β , φ and γ of these forces are all measured counterclockwise starting from the positive \bar{x} axis.

Appendix B

Though we have explained that the theoretical contact angle in the pseudo-solid approach is naturally 180° , there still exists an important problem. There is a very thin gas film (with its thickness negligible) between the superhydrophobic cylinder and the liquid in the numerical simulations, while this gas film may not necessarily be maintained in reality. For the cases with and without the thin gas film, why do the motions of the impacting superhydrophobic cylinder (or sphere in Galeano-Rios *et al.* 2021) agree well with each other? This will be explained from the perspective of energy.

When there is no gas film between the cylinder and the liquid, the sum of surface energies of the whole system can be expressed as

$$E = \Sigma_{sg}\sigma_{sg} + \Sigma_{lg}\sigma_{lg} + \Sigma_{sl}\sigma_{sl}, \quad (\text{B1})$$

where Σ_{sg} , Σ_{lg} and Σ_{sl} denote the areas of the solid–gas interface, the liquid–gas interface and the solid–liquid interface, and σ_{sg} , σ_{lg} and σ_{sl} are the three corresponding surface energy per area.

When there is a very thin gas film between the cylinder and the liquid (considering the same configurations as in (B1)), the solid–liquid interface with area Σ_{sl} mentioned above becomes the liquid–gas interface and the solid–gas interface. Thus, the sum of surface energies of the whole system becomes

$$E' = \Sigma_{sg}\sigma_{sg} + \Sigma_{lg}\sigma_{lg} + \Sigma_{sl}(\sigma_{sg} + \sigma_{lg}). \quad (\text{B2})$$

According to the well-known Thomas Young’s relation, the contact angle can be expressed as

$$\cos \theta = \frac{\sigma_{sg} - \sigma_{sl}}{\sigma_{lg}}. \quad (\text{B3})$$

When the contact angle θ of the solid (e.g. the pseudo-solid in this paper) is equal to 180° , we have the following relationship from (B3):

$$\sigma_{sl} = \sigma_{sg} + \sigma_{lg}. \quad (\text{B4})$$

Resurrection of a superhydrophobic cylinder

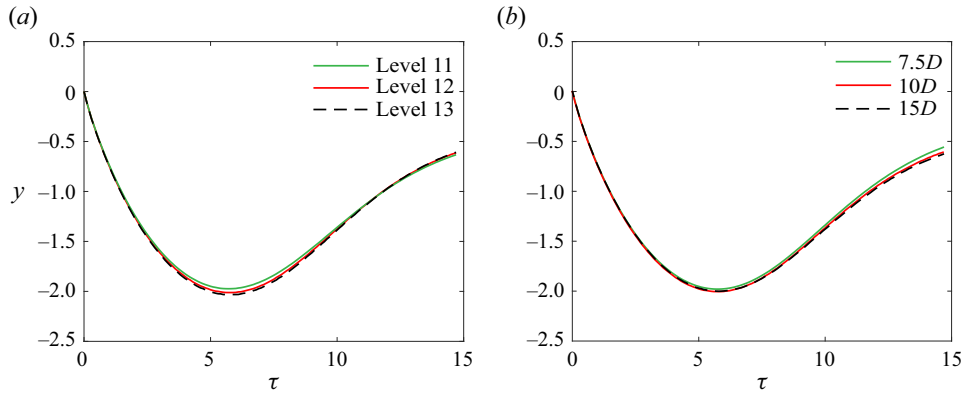


Figure 12. Trajectory of the lowest point on the cylinder under different (a) grid refinement level and (b) width of the computational domain. The parameters are given as $We_l = 15$ and $\lambda_\rho = 1.2$ (other parameters are listed in table 1).

With (B4), it can be found that the sum of surface energies of the whole system is the same whether there is a very thin film or not (i.e. $E = E'$) when $\theta = 180^\circ$. The surface energies govern the surface tension effect on the cylinder, and the surface tension forces are related the first variations of the surface energies (Kralchevsky *et al.* 1993). Therefore, it is demonstrated why the liquid-entry behaviour of a superhydrophobic solid is less dependent on the microscopic details of the contact with the solid surface.

Appendix C

The grid independence analysis and the domain-size independence analysis are conducted in this appendix. As shown in figure 12(a), the simulations of different minimum mesh sizes are performed for a computational domain spanning $10D$ in width and $20D$ in length (as in figure 1). It is found that the maximum grid refinement of level 12 (i.e. the minimum grid size of $10D/2^{12}$) is sufficient for the numerical simulations by comparisons with the cases of levels 11 and 13. Thus, the grid refinement of level 12 is adopted in our simulations. In order to obtain the appropriate size of the computational domain, we compare the numerical results for the widths of $7.5D$, $10D$ and $15D$ (with the length–width ratio fixed at 2 as in figure 1) in figure 12(b). The numerical results for the width of $10D$ are very close to those for the width of $15D$, which shows that the width of $10D$ is large enough for the computational domain for the numerical simulations. Thus, the computational domain that spans $10D$ in width and $20D$ in length is adopted in our simulations.

It is worth noting that, when the physical parameters of a simulation case are very close to the limits of the parameter regimes (see the demarcation curves of the phase diagram in figure 5), the fate of the impacting cylinder can possibly change significantly with a very slight disturbance in both physical and computational parameters (e.g. from sinking to resurrecting, see the snapshots in figure 3c,d). For example, in a case with physical parameters very close to the demarcation of regimes of sinking and resurrecting, a change in the minimum mesh size (e.g. from the maximum refinement level 11 to 12) may cause a significant difference for the trajectory of the impacting cylinder, which seemingly leads to a bad result for the convergence test on grid independency. However, for the cases with physical parameters a little far from the demarcation, the grid independency is easy to verify (see e.g. figure 12). Furthermore, when exploring the critical Weber numbers for different regimes (with other physical parameters the same, see figure 5), the critical values

of We_l obtained under two different refinement levels may be different but the difference is very slight (typically, much less than 1). This indicates that our numerical results are relatively reliable though the discussed impacting behaviour can be very sensitive to parameters.

REFERENCES

- BARBOT, A., TAN, H., POWER, M., SEICHEPINE, F. & YANG, G.-Z. 2019 Floating magnetic microrobots for fiber functionalization. *Sci. Robot.* **4**, eaa8336.
- BASUALDO, F.N.P., BOLOPION, A., GAUTHIER, M. & LAMBERT, P. 2021 A microrobotic platform actuated by thermocapillary flows for manipulation at the air–water interface. *Sci. Robot.* **6**, eabd3557.
- BHATNAGAR, R. & FINN, R. 2006 Equilibrium configurations of an infinite cylinder in an unbounded fluid. *Phys. Fluids* **18**, 047103.
- BOWDEN, N., TERFORT, A., CARBECK, J. & WHITESIDES, G.M. 1997 Self-assembly of mesoscale objects into ordered two-dimensional arrays. *Science* **276**, 233–235.
- BUSH, J.W.M. & HU, D.L. 2006 Walking on water: biocomotion at the interface. *Annu. Rev. Fluid Mech.* **38**, 339–369.
- CHEN, H., LIU, H.-R., LU, X.-Y. & DING, H. 2018 Entrapping an impacting particle at a liquid–gas interface. *J. Fluid Mech.* **841**, 1073–1084.
- CHEN, H. & SIEGEL, D.J. 2018 A floating cylinder on an unbounded bath. *J. Math. Fluid Mech.* **20**, 1373–1404.
- CIMPEANU, R. & MOORE, M.R. 2018 Early-time jet formation in liquid–liquid impact problems: theory and simulations. *J. Fluid Mech.* **856**, 764–796.
- COINTE, R. & ARMAND, J.L. 1987 Hydrodynamic impact analysis of a cylinder. *ASME J. Offshore Mech. Arc. Engrg* **109**, 237–243.
- COLICCHIO, G., GRECO, M., MIOZZI, M. & LUGNI, C. 2009 Experimental and numerical investigation of the water-entry and water-exit of a circular cylinder. In *The 24th International Workshop on Water Waves and Floating Bodies, Zelenogorsk, Russia*, 19–22 April.
- GALEANO-RIOS, C.A., CIMPEANU, R., BAUMAN, I.A., MACEWEN, A., MILEWSKI, P.A. & HARRIS, D.M. 2021 Capillary-scale solid rebounds: experiments, modelling and simulations. *J. Fluid Mech.* **912**, A17.
- GOHARZADEH, A. & MOLKI, A. 2012 Experimental study of water entry and exit of a circular cylinder at free surface. In *Proceedings of the ASME 2012 International Mechanical Engineering Congress and Exposition, IMECE2012*, Texas, USA, pp. 329–335.
- GREENHOW, M. 1988 Water-entry and -exit of a horizontal circular cylinder. *Appl. Ocean Res.* **10** (4), 191–198.
- GREENHOW, M. & LIN, W.-M. 1983 Nonlinear free surface effects: experiments and theory. *MIT Internal Rep.* 83-19.
- HAFSIA, Z., MNASRI, C., MOHAMED, O. & MAALEL, K. 2009 Water entry and exit of horizontal cylinder in free surface flow. In *CONV-09. Proceedings of International Symposium on Convective Heat and Mass Transfer in Sustainable Energy*, 26 April–1 May, Hammamet, Tunisia.
- HOWISON, S.D., OCKENDON, J.R. & WILSON, S.K. 1991 Incompressible water-entry problems at small deadrise angles. *J. Fluid Mech.* **222**, 215–230.
- HU, D.L., CHAN, B. & BUSH, J.W.M. 2003 The hydrodynamics of water strider locomotion. *Nature* **424**, 663–666.
- HU, W., LUM, G.Z., MASTRANGELI, M. & SITTI, M. 2018 Small-scale soft-bodied robot with multimodal locomotion. *Nature* **554**, 81–85.
- HUNT, R., ZHAO, Z., SILVER, E., YAN, J., BAZILEVS, Y. & HARRIS, D.M. 2023 Drag on a partially immersed sphere at the capillary scale. *Phys. Rev. Fluids* **8** (8), 084003.
- IRANMANESH, A. & PASSANDIDEH-FARD, M. 2017 A three-dimensional numerical approach on water entry of a horizontal circular cylinder using the volume of fluid technique. *Ocean Engrg* **130**, 557–566.
- JANSSENS, S., CHAURASIA, V. & FRIED, E. 2017 Effect of a surface tension imbalance on a partly submerged cylinder. *J. Fluid Mech.* **830**, 369–386.
- JI, B., SONG, Q. & YAO, Q. 2017 Numerical study of hydrophobic micron particle's impaction on liquid surface. *Phys. Fluids* **29** (7), 077102.
- JUNG, D., *et al.* 2021 Highly conductive and elastic nanomembrane for skin electronics. *Science* **373**, 1022–1026.
- KIARA, A., PAREDES, R. & YUE, D.K.P. 2017 Numerical investigation of the water entry of cylinders without and with spin. *J. Fluid Mech.* **814**, 131–164.

Resurrection of a superhydrophobic cylinder

- KIM, S.J., HASANYAN, J., GEMMELL, B.J., LEE, S. & JUNG, S. 2015 Dynamic criteria of plankton jumping out of water. *J. R. Soc. Interface* **12** (111), 20150582.
- KOH, J.S., YANG, E., JUNG, G.P., JUNG, S.P., SON, J.H., LEE, S.I., JABLONSKI, P.G., WOOD, R.J., KIM, H.Y. & CHO, K.J. 2015 Jumping on water: surface tension-dominated jumping of water striders and robotic insects. *Science* **349**, 517–521.
- KOROBKIN, A.A. 1997 Asymptotic theory of liquid–solid impact. *Phil. Trans. R. Soc. A* **355**, 507–522.
- KRALCHEVSKY, P.A., PAUNOV, V.N., DENKOV, N.D., IVANOV, I.B. & NAGAYAMA, K. 1993 Energetical and force approaches to the capillary interactions between particles attached to a liquid–fluid interface. *J. Colloid Interface Sci.* **155**, 420–437.
- LEE, D.G. & KIM, H.Y. 2008 Impact of a superhydrophobic sphere onto water. *Langmuir* **24**, 142–145.
- LIN, P. 2007 A fixed-grid model for simulation of a moving body in free surface flows. *Comput. Fluids* **36**, 549–561.
- LIU, H.-R., GAO, P. & DING, H. 2017 Fluid–structure interaction involving dynamic wetting: 2D modeling and simulations. *J. Comput. Phys.* **348**, 45–65.
- LYU, X., WEI, Z., TANG, H., NEW, T.H. & LI, H. 2015 On the motion of a falling circular cylinder in flows after water entry. In *Proceedings of SPIE International Conference on Experimental Mechanics 2014*, vol. 9302, 930233.
- MARSTON, J.O., LI, E.Q. & THORODDSEN, S.T. 2012 Evolution of fluid-like granular ejecta generated by sphere impact. *J. Fluid Mech.* **704**, 5–36.
- PIERSON, J.-L. & MAGNAUDET, J. 2018 Inertial settling of a sphere through an interface. Part 1. From sphere flotation to wake fragmentation. *J. Fluid Mech.* **835**, 762–807.
- POPINET, S. 2003 Gerris: a tree-based adaptive solver for the incompressible Euler equations in complex geometries. *J. Comput. Phys.* **190**, 572–600.
- POPINET, S. 2009 An accurate adaptive solver for surface-tension-driven interfacial flows. *J. Comput. Phys.* **228**, 5838–5866.
- THORODDSEN, S.T., ETOH, T.G., TAKEHARA, K. & TAKANO, Y. 2004 Impact jetting by a solid sphere. *J. Fluid Mech.* **499**, 139–148.
- TRUSCOTT, T.T., EPPS, B.P. & BELDEN, J. 2014 Water entry of projectiles. *Annu. Rev. Fluid Mech.* **46**, 355–378.
- UEDA, Y., TANAKA, M., UEMURA, T. & IGUCHI, M. 2010 Water entry of a superhydrophobic low-density sphere. *J. Vis.* **13**, 289–292.
- VELLA, D. 2015 Floating versus sinking. *Annu. Rev. Fluid Mech.* **47**, 115–135.
- VELLA, D., LEE, D.-G. & KIM, H.-Y. 2006 Sinking of a horizontal cylinder. *Langmuir* **22**, 2972–2974.
- VELLA, D. & LI, J. 2010 The impulsive motion of a small cylinder at an interface. *Phys. Fluids* **22**, 052104.
- VELLA, D. & METCALFE, P.D. 2007 Surface tension dominated impact. *Phys. Fluids* **19**, 072108.
- WAGNER, H. 1932 Über Stoss- und Gleitvorgänge an der Oberfläche von Flüssigkeiten. *Z. Angew. Math. Mech.* **12**, 193–215.
- WEI, Z. & HU, C. 2014 An experimental study on water entry of horizontal cylinders. *J. Mar. Sci. Technol.* **19**, 338–350.
- WHITE, F.M. 2016 *Fluid Mechanics*, 8th edn. McGraw-Hill.
- ZHANG, W. & ZHOU, X. 2023 Equilibria and stabilities of a confined floating cylinder. *J. Fluid Mech.* **954**, A22.
- ZHAO, R. & FALTINSEN, O. 1993 Water entry of two-dimensional bodies. *J. Fluid Mech.* **246**, 593–612.
- ZHU, X., FALTINSEN, O.M. & HU, C. 2007 Water entry and exit of a horizontal circular cylinder. *J. Offshore Mech. Arctic Engng* **129**, 253–264.